Supplementary Materials for

Enhanced East Pacific Rise hydrothermal activity during the last two glacial terminations

D. C. Lund,* P. D. Asimow, K. A. Farley, T. O. Rooney, E. Seeley, E. W. Jackson, Z. M. Durham

*Corresponding author. E-mail: david.lund@uconn.edu

Published 29 January 2016, *Science* **351**, 478 (2016)
DOI: 10.1126/science.aad4296

This PDF file includes:

Materials and Methods
Supplementary Text
Figs. S1 to S11
Full Reference List
Captions for Tables S1 to S5

Other Supplementary Material for this manuscript includes the following:
(available at www.sciencemag.org/content/351/6272/478/suppl/DC1)

Tables S1 to S5 as Excel files

Materials and Methods

Age models

Age control for the EPR cores is provided by stable isotope and radiocarbon analyses of planktonic foraminifera (*G. ruber*, > 250 μm size fraction). Ages for the long cores at 11ºS (Y71-07-47 and Y71-07-53) were determined by correlation of their planktonic $\delta^{18}O$ stratigraphy to the global benthic $\delta^{18}O$ stack of ref. *30* (Table S2). We followed a similar approach for KLH068 and KLH093 at 1ºN (*12*). Ages for Y71-09-115 were determined by correlation of its $\delta^{18}O$ record to the radiocarbon-constrained $\delta^{18}O$ records of nearby core Y71-09-106. The approximate calendar age uncertainty for each $\delta^{18}O$-based tie point is ±3-4 kyr.

Oxygen isotope analyses of planktonic foraminifera (*G. ruber*) were made using a Finnigan MAT253 coupled to a Kiel IV automated carbonate device. Samples run at the University of Michigan (n=225) were corrected to Vienna Pee-Dee Belemnite (VPDB) using NBS-19 (n=38, $\delta^{18}O$=-2.19±0.05‰, $\delta^{13}C$=1.93±0.05‰) and NBS-18 (n=26, $\delta^{18}O$=-22.99±0.04‰, $\delta^{13}C$=-5.01±0.03‰). Samples run at Georgia Tech (n=19) were converted to VPDB via NBS-19 (n=2, $\delta^{18}O$=-2.19±0.08‰, $\delta^{13}C$=1.93±0.01‰) and an in-house standard with similar isotopic composition (n=12, $\delta^{18}O$=-2.05±0.07‰, $\delta^{13}C$=2.15±0.02‰).

Radiocarbon ages were determined for two cores at 6ºS (Y71-09-104 and Y71-09-106) and two cores at 11ºS (Y71-07-49 and Y71-07-51). Each ^{14}C age was converted to

calendar ages using Calib 7.1 assuming a surface water reservoir age of 400±200 years (http://calib.qub.ac.uk/ calib/). The typical calendar age uncertainty for each ^{14}C control point is ±1-2 kyr (Table S1). In lower sedimentation rate cores like those on the EPR (2-3 cm/kyr), bioturbation may introduce age error of several thousand years for individual control points (*30*), even in cases where the oxygen isotope stratigraphy shows no signs of bioturbation (*32*). For cores that lack obvious age reversals (Y71-09-104, Y71-09-106, and Y71-07-51), we therefore determine the age model by linear fit to the ^{14}C ages for each core. In the case of core Y71-09-104, the primary decrease in $\delta^{18}O$ occurred after 14 kyr BP, about 4 kyr later than nearby core Y71-09-106 (Figure 2) and other eastern tropical Pacific locations (*33*). The age offset is most likely due to the single age control point at 13.9 kyr BP (Table S1), which is ~3 kyr younger than predicted by a linear fit to other ages in the same core. Thus, even in cases ^{14}C ages increase monotonically, individual radiocarbon control points may have errors approaching that for oxygen isotope stratigraphy. In core Y71-07-49, there is a clear age reversal prior to 40 kyr BP (Table S1) and as a result these points were excluded from the age model.

Metal concentrations

Metal analyses of samples for cores Y71-09-115 and Y71-07-47 were performed using a Bruker Pioneer S4 XRF at Michigan State University (MSU) (*34*). The relative standard deviation for major elements in external standards USGS BHVO-1 and RGM-1 is <0.3%. Analyses of Y71-09-104, Y71-09-106, Y71-07-49, and Y71-07-51 were performed using laser ablation and a Thermo-Fisher ICAP Q ICP-MS at MSU. Relative standard deviations and accuracy for major elements are ~3%. The calibration for As

was obtained using NIST 612 and GSD-1G, JB1a, and JA3 standards, with accuracy within ±5% of accepted values. The GSE-1G standard was run as an unknown for quality control; the mean of 4 measurements on 4 separate analytical sessions was within 5% of accepted value, with a relative standard deviation of <5%. Arsenic relative standard deviation among sample replicates was 2-10%, depending on absolute As concentrations. ICP-MS data for Y71-07-53 were reported in (*16*) and assigned ages based on the $\delta^{18}O$ stratigraphy developed for this work.

Fe and Mn concentrations were corrected for detrital inputs using Ti and the average Fe/Ti and Mn/Ti ratio of EPR basalts (*35*). The detritial contributions were determined by multiplying the Ti concentration of each sediment sample by the Fe/Ti (8.1±0.3) and Mn/Ti (0.1±0.01) of recent (0 to 0.12 Ma) EPR basalts (*36*). The resulting detrital value was then substracted from the total Fe or Mn concentration to isolate the hydrothermal component. Detrital Fe corrections were typically 0.5% or less (by weight) (Figures S5 and S6). Mn corrections were negligible, typically 0.005% or less, and are therefore not shown.

Flux estimates

Fluxes of hydrothermal components were estimated using both mass accumulation rates (MAR) and the ^{3}He normalization method. MAR's were determined using the dry-bulk density (DBD) of each sample, estimated using %CaCO3 (*37*), and the sedimentation rate. Because sedimentation rates are based on the assigned age model, MAR's are sensitive to age uncertainty. We assume an age error of ±20% between

successive metal analyses, larger than either the DBD uncertainty (±3%) or the error associated with the metal analyses (typically 5% or less). The age uncertainty is the primary contributor to the metal flux errors depicted in Figures 2 and 3. Prior to combining the short and long records at 11ºS into a continuous time series (Figure 4), we normalized each record by subtracting the mean flux and dividing by the standard deviation. This was necessary because the shorter records are closer to the ridge crest (Figure 1) and as a result have higher mean metal concentrations and fluxes. For both the western and eastern flank records in Figure 4, the 0-40 kyr BP interval is based on data from the shorter gravity cores while the interval prior to 40 kyr BP is based on data from the longer piston cores.

We also estimated sediment flux for two cores (Y71-07-49 and Y71-09-106) using the ^{3}He normalization method. The primary benefit of this approach is that: 1) it is insensitive to age model uncertainty, and 2) it yields discrete estimates of sediment flux at each stratigraphic level. Sediment fluxes (in units of g cm^{-2} yr^{-1}) are determined by dividing the extraterrestrial ^{3}He flux ([1.0±0.2] x 10^{-15} cm^{3} STP cm^{-2} yr^{-1}) (*38*) by the concencentration of ^{3}He at each depth in the core (in cm^{3} STP g^{-1}) (*39*). Helium concentrations and isotopic composition were determined at the Caltech Noble Gas Laboratory following the methods outlined in ref. *40* (Table S4). We assume retention of ^{3}He in EPR sediments is constant over the last glacial cycle. Fe and Mn accumulation rates for cores Y71-09-106 and Y71-07-49 were calculated by multiplying the non-carbonate sediment flux by %Fe (cfb) and %Mn (cfb) (Figure S1). Sediment focusing factors were determined by dividing the measured and predicted ^{3}He inventory for

discrete intervals within each core (Figure S3). Predicted ^{3}He inventories are based on the extraterrestrial ^{3}He flux multiplied by the time between radiocarbon-based calendar ages. The uncertainty in the predicted inventories takes into account analytical error in the ^{14}C measurements but does not account for potential age biases due to bioturbation.

Supplementary Text

Age offsets between time series

Table S5 summarizes the time offsets between different metal flux time series within each core and between different cores. The maximum linear correlation was determined by shifting the time series past one another in 1 kyr increments. Each cell in Table S5 includes the time offset with the highest correlation (in kyr) and the corresponding correlation coefficient (r). For example, the maximum correlation between inferred Mn and Fe fluxes in core KLH068 at 1ºN occurs at an offset of 2 kyr, with an r of 0.80 (cell B6). For core KLH093, the maximum correlation occurs when the Mn and Fe time series are offset by 0 kyr (cell E6). The maximum correlation between Fe flux in the two cores occurs at 0 kyr (cell B11). We observe similar offsets for the other 1ºN comparisons (maximum of 2 kyr). At 6ºS, the maximum correlation coefficient for metal fluxes within each core occurs at offsets of 0-1 kyr. Between cores, the offsets are slightly higher, ranging from 2-4 kyr for cores 104 and 106 (cells B26:D28), 1-2 kyr for cores 106 and 115 (cells G26:H27), and 1-2 kyr for cores 104 and 115 (cells K26:L27). These offset are generally consistent with the expected timing errors for radiocarbon dates in cores with sedimentation rates of 2-3 cm/kyr (see Methods section). At 11ºS, the

maximum correlation for elements within each core occurs at offsets of 0-1 kyr. The highest correlations between cores 49 and 51 occur at offsets of 0-3 kyr (cells B42:D44). For cores 47 and 43, which are the cores that span Termination II, the offsets are 2-3 kyr (G42:H43). These offsets are consistent with the expected errors associated with oxygen isotope stratigraphy (3-4 kyr).

In addition to comparing between cores at the same latitude, it is instructive to compare cores across latitudes. To simplify the discussion, we focus on comparing the same element between different cores. The maximum correlation between core 106 at 6ºS and core 51 at 11ºS occurs at a range of offsets, ranging from 0-4 kyr for Fe, 0-3 kyr for Mn, and 0-3 kyr for As (cells B53:D55). The broader range of values occurs because when core 51 is shifted younger, the main increase in metal flux in the two cores is better aligned, but then the high metal flux in the youngest part of core 51 is matched with decreasing fluxes in core 106. The net effect is similar correlation coefficients across a range of offsets. The comparison between cores 106 and 49 (cells B58:D60) and cores 104 and 51 (cells B63:D65) yields slightly higher offsets, typically 3-5 kyr. We observe the largest apparent offsets between cores 104 and 49 (cells B68:D70). In this case, the maximum correlation between the Fe time series occurs at an offset of 6-8 kyr. For Mn, it is 4-6 kyr and for As it is 6-8 kyr. This appears to driven in part by the anomalously young radiocarbon age in core 104 at ~14 kyr BP which causes its oxygen isotope stratigraphy during the last deglaciation to lag other cores at 6ºS by 4-5 kyr (Figure 2). Age offsets between core KLH093 at 1ºN and core Y71-09-104 range from 2-5 kyr (cells B78:C79). Comparing KLH093 to cores 106, 115, 51, and 49, we find smaller offsets.

Therefore in most cases the age offsets among cores at different latitudes is 5 kyr or less, similar to what would be expected given the uncertainty in the age models and the mass accumulation rate method.

Fe/Mn ratios and diagenetic overprinting

Core top (i.e. late Holocene) sediments along the EPR ridge crest are characterized by Fe/Mn ratios of 3.5±1.8 (2σ) (*8*). Subsequent investigators found a similar Fe/Mn ratio in EPR sediments (*9, 16, 35, 41, 42*). Fe/Mn ratios for the cores discussed in this paper are shown in Figure S7. The highest values occur in the equatorial Pacific locations. Prior to 20 kyr BP, Fe/Mn ratios >10 at the 1°N sites suggest that solid-phase Mn has been remobilized. After 20 kyr BP, the Fe/Mn ratio varies between 4 and 6, within the range outlined by Dymond (*8*). The lack of anomalously low Fe/Mn values in the upper portion of the cores suggests that the majority of dissolved Mn from deeper in the section diffused out of the sediments rather than being precipitated as MnO_2. Although suboxic diagenesis likely influenced Mn, the Fe results at 1°N are consistent with locations further south, suggesting that hydrothermal input, as opposed to diagenesis, was the primary driver of the Fe signal.

At 6°S, Fe/Mn ratios are lower than at 1°N, ranging from 3 to 10 (Figure S7). The decrease in Fe/Mn ratios parallels the latitudinal trend in sedimentary biogenic opal content (*8*), implying that lower export productivity results in less diagenetic influence on solid-phase Mn at 6°S. Similar to the 1°N sites, the Fe/Mn ratio in two cores at 6°S (Y71-09-104 and Y71-09-106) is higher before 20 kyr BP than afterwards, implying that

some diagenetic remobilization of Mn may have occurred. The third core (Y71-09-115) has Fe/Mn values of 5.3±2.6 (2σ) and lacks any clear temporal trend. The overall agreement between Fe, Mn, and As fluxes at 6°S suggests that hydrothermal input was the primary driver. If diagenesis played a dominant role in the setting the profiles, we would instead expect to find peaks in Fe and Mn offset in depth given the constrast in their redox potential (*17*).

Fe/Mn ratios at 11°S are systematically lower than those at 6°S and generally consistent with hydrothermal input. The mean Fe/Mn for the cores is 3.7±0.8 (Y71-07-47), 3.5±0.7 (Y71-07-49), 3.5±0.7 (Y71-07-51), and 4.8±1.6 (Y71-07-53). The somewhat higher Fe/Mn ratio for Y71-07-53 implies that Mn remobilization may have occurred at this site. Rhenium is at detrital levels in Y71-07-53, however, implying that reducing conditions were not sufficient to mobilize Fe (*16, 43*). Low organic carbon concentrations in Y71-07-53 also imply that suboxic diagenesis is an unlikely driver of down core Fe variability (*16*). For example, Fe levels reach 10% of the total sediment weight during Termination II, which spans approximately 15 cm of core depth. If the required C_{org} originated from this interval, the amount necessary for reducing Fe would be ~0.6%. Given measured C_{org} values of ~0.2% (*16*), the initial required C_{org} concentration would be 0.8%. If the Fe originated from a larger 30 cm interval, then the required initial amount would be 0.5%. These estimates are at least twice any measured C_{org} concentration in Y71-07-53 (*16*). In locations such as the Guatemala Basin where C_{org} levels approach 1% and oxygen demand is high, there is clear evidence for Mn remobilization (*48*). Even at the organic carbon-rich Guatemala Basin sites, however,

there is no indication that Fe has been remobilized and focused at the same stratigraphic level as Mn. The overall lack of evidence for Fe remobilization at the southern EPR sites is consistent with low sedimentary organic carbon concentrations in ridge crest sediments from 10ºS to 20ºS (9, *42, 45*) and the progressive decrease in biogenic opal content from the equator to the oligotrophic subtropical gyre (*8*).

Extended hydrothermal record

The one other detailed time series of EPR hydrothermal sedimentation in the published literature is core GS7202-35, recovered from 80 km west of the EPR at 15ºS (*42*). The record spans 740 kyr and has been dated using oxygen isotope stratigraphy. The average Fe/Mn for GS7202-35 is 2.6±0.6 (2σ), generally lower than the 6ºS and 11ºS cores. Although Fe/Mn ratios in GS7202-35 approach 3.5 at glacial terminations, the average Fe/Mn is at the low end of the range reported by Dymond (1981) for core top sediments. Generally lower Fe/Mn values may be due to enhanced input of Mn and S-rich plume particles related to superfast spreading at 15ºS (*42*). Given the oligotrophic location and low organic carbon concentrations in core GS7202-35 (<0.2%), glacial-interglacial variability in metal concentrations are apparently due to cyclical variations in hydrothermal input with diagenetic modification due to changes in bottom water oxygen concentration (*42*).

To test the bottom water O_2 hypothesis, redox-sensitive U/Fe and P/Fe ratios from GS7202-35 were compared to those from Y71-07-53 (*42*). At the time, core Y71-07-53 lacked age control, making it difficult to infer whether there were coherent regional

changes in the oxygen sensitive proxies. Here we apply the new age model for Y71-07-53 to re-evaluate the relative timing of U/Fe and P/Fe variability (Figure S8). We find that peak P/Fe ratios in Y71-07-53 occur during MIS 5 while those in GS7202-35 occur during MIS 6 (Figure S8, bottom panel). Given that there is little common signal in the U/Fe ratios in the cores (Figure S8, top panel), the results suggest that a process other than regional changes in bottow water O_2 drove P/Fe and U/Fe variability.

The concentration of individual hydrothermal metals in core GS7202-35, expressed on a carbonate-free basis, vary on glacial-interglacial timescales (Figure S9). Given the sedimentation rate (average 1.3 cm/kyr) and sampling resolution (average 4 kyr) in GS7202-35, it is unclear whether metal concentrations peak during glacial terminations. Nevertheless, Fe, Mn, and V show coherent down-core variability, with concentration minima generally occurring during even (i.e. glacial) marine isotope stages. Normalized metal concentrations also show a high degree of similarity to the bathymetry record of Tolstoy (2015) (Figure S10). Large temporal offsets between the records prior to 400 kyr BP are most likely related to the limited age control for the bathymetry. Spectral analysis of the GS7202-35 records indicates the Fe and V are characterized by dominant periods near 100 kyr and 40 kyr (Figure S11). The spectral peaks at 23 kyr lack statistical significance, perhaps due to the 4 kyr sampling resolution. The Mn power spectrum also has a peak centered at 100 kyr, with a second broad peak between 40 kyr and 20 kyr. These results suggest that input of hydrothermal Fe, V, and Mn to this site varied on Milankovitch timescales, consistent with the data from 1ºN, 6ºS, and 11ºS.

Additional long-term records are necessary to determine if Milankovitch-scale periodicities are present in proxies of hydrothermal activity at other locations on the EPR.

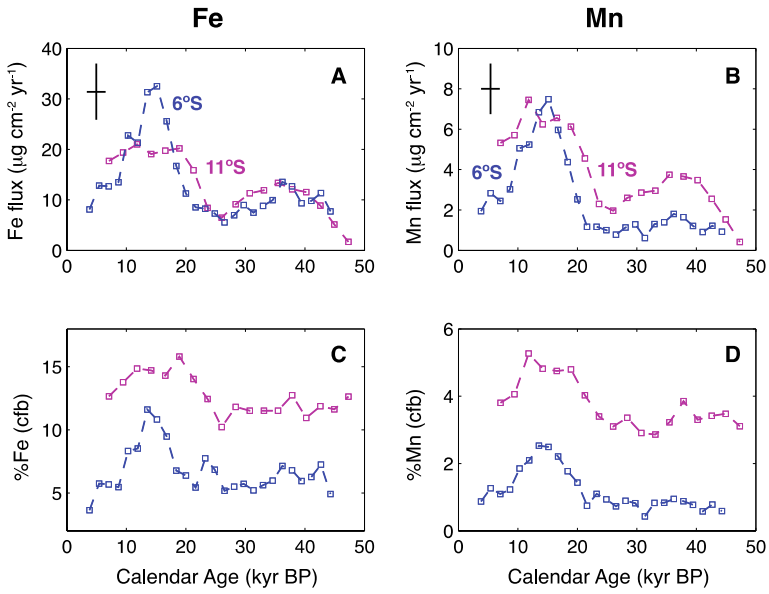

Fig. S1.

^{3}He-normalized metal fluxes and metal concentrations for two cores, including Y71-09-106 at 6ºS (blue) and Y71-07-49 at 11ºS (magenta). A) ^{3}He-normalized Fe fluxes, B) ^{3}He-normalized Mn fluxes, C) %Fe on a carbonate-free basis (cfb), and D) %Mn (cfb). In each case, the time series have been corrected for detrital contributions (see Methods). Accumulation rates were estimated using an extraterrestrial ^{3}He flux of [1.0±0.2] x 10^{-15} cm^{3} STP cm^{-2} yr^{-1} (*38*) and sedimentary ^{3}He concentrations. Due to point to point variability in ^{3}He concentrations (Table S4), the flux estimates are based on a 3-point running mean. The uncertainties in the metal fluxes (cross symbols) reflect the age model error (x-axis) and the combined uncertainty of the extraterrestrial ^{3}He flux and variability in sample ^{3}He concentrations (y-axis).

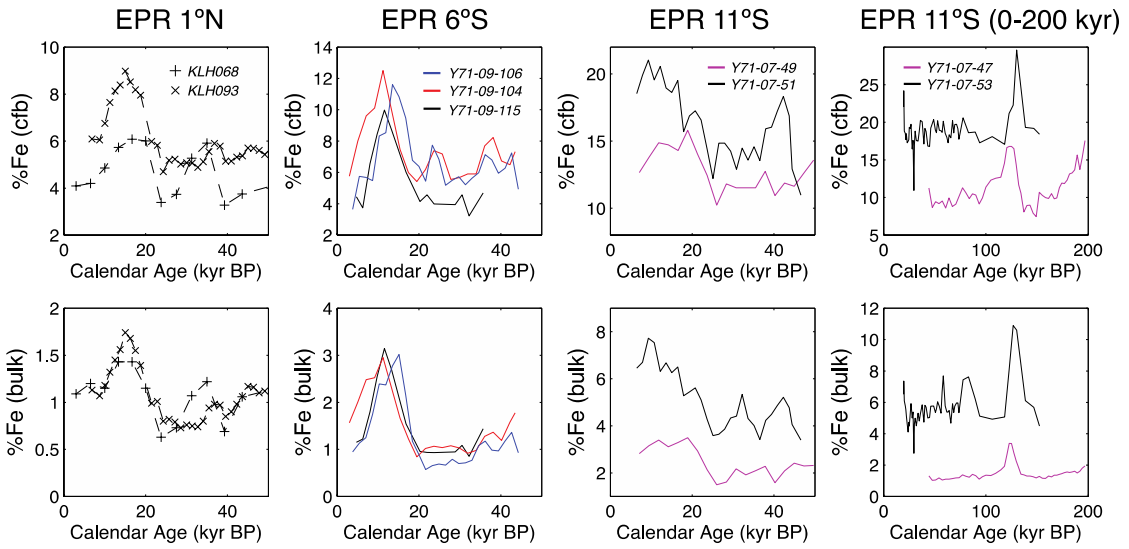

Fig. S2

Carbonate-free Fe (top row) and bulk Fe (bottom row) concentrations for the cores discussed in this work, including cores from 1ºN (*12*) (first column), 6ºS (second column), 11ºS (third column), and the 0-200 kyr BP records at 11ºS (fourth column). Both carbonate free and bulk values have been corrected for detrital inputs (see Methods for details).

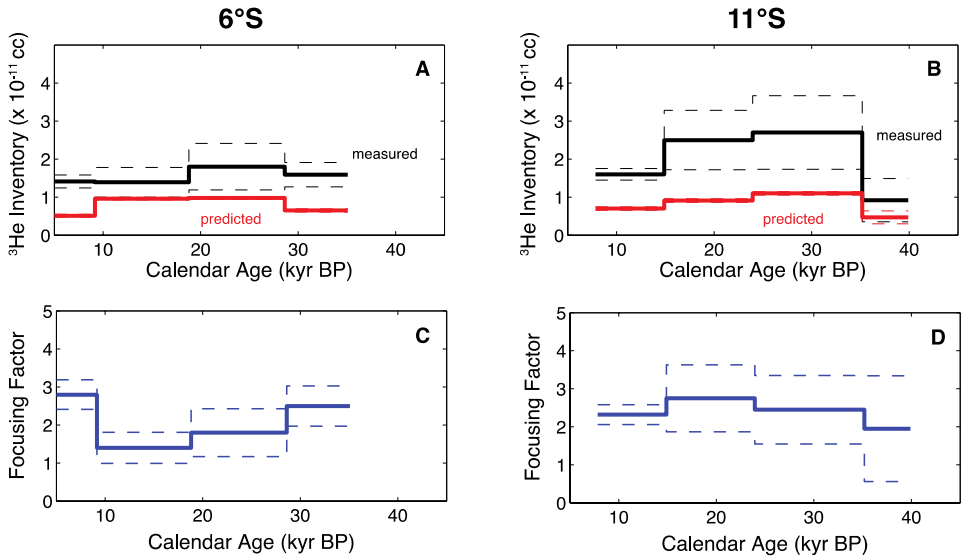

Fig. S3

^{3}He inventories and focusing factors for core Y71-09-106 at 6ºS and core Y71-07-49 at 11ºS. A) Measured (black) and predicted (red) ^{3}He inventories for the 6ºS site. Predicted inventories are based on an assumed extraterrestrial ^{3}He flux of $1x10^{-15}$ cm^3 STP cm^{-2}yr^{-1} (*38*) multiplied by the time between ^{14}C-based calendar ages. B) Measured (black) and predicted (red) ^{3}He inventories for the 11ºS site. C) Focusing factors for the 6ºS site, based the ratio of the measured to predicted ^{3}He inventory. D) Focusing factors for the 11ºS site. Ratios greater than unity indicate that horizontal focusing occurred. Neither core displays anomalous levels of focusing during the last deglaciation (10-20 kyr BP).

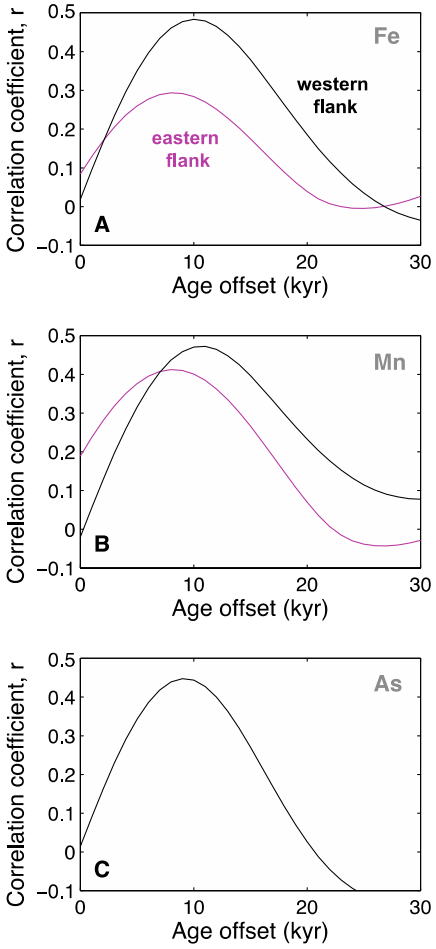

Fig. S4

Linear correlation coefficients for the EPR hydrothermal fluxes and bathymetry time series in Figure 4, including Fe (panel A), Mn (panel B), and As (panel C). Results for both western flank (black) and eastern flank records (magenta) are shown. The age offset between hydrothermal and bathymetry time series was systematically varied to determine the maximum correlation coefficient (r) between the records. The maximum correlation occurs when ages for the bathymetry are increased by 9±1 kyr.

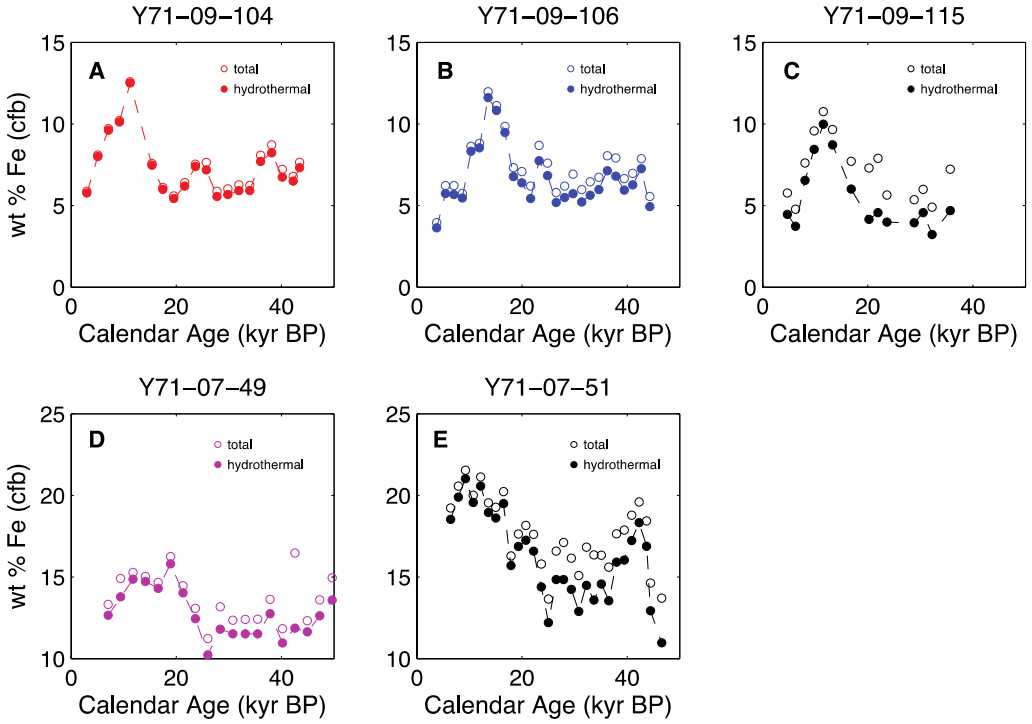

Fig. S5

Plots of total Fe and hydrothermal Fe for cores at 6ºS (panels A, B, C) and 11ºS (panels D, E). The detrital Fe contribution was determined by multiplying the Ti concentration in each sample by the Fe/Ti ratio of EPR basalts (*35*). We used data from basalts 0.12 Ma and younger (Fe/Ti =8.1±0.1) (*36*). The hydrothermal component was determined by subracting detrital Fe from total Fe. A similar procedure was followed for Mn using the Mn/Ti ratio of the same EPR basalts (0.1±0.01). The Mn results are not shown because the corrections were imperceptible.

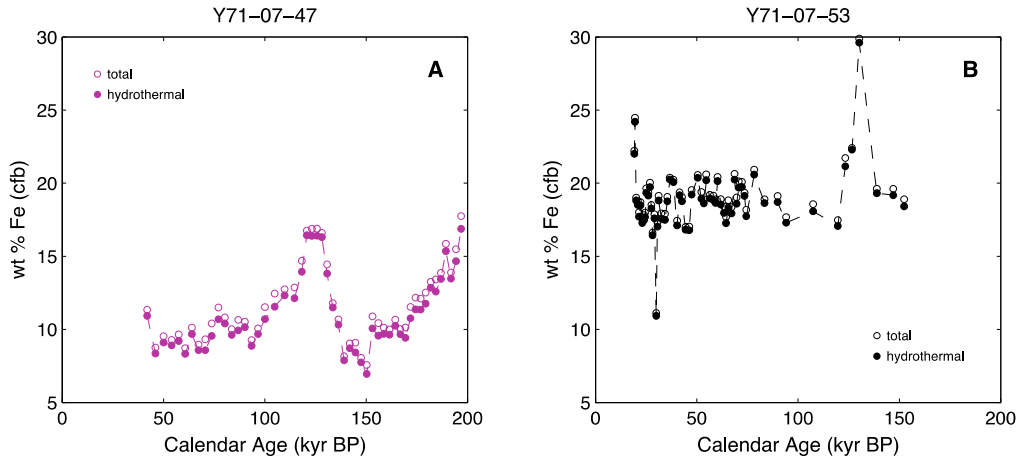

Fig. S6

Total Fe and hydrothermal Fe for the two longer records at 11ºS. A) Results for core Y71-07-47 (eastern flank), B) Results for core Y71-07-53 (western flank). See Figure S5 caption for description of detrital correction.

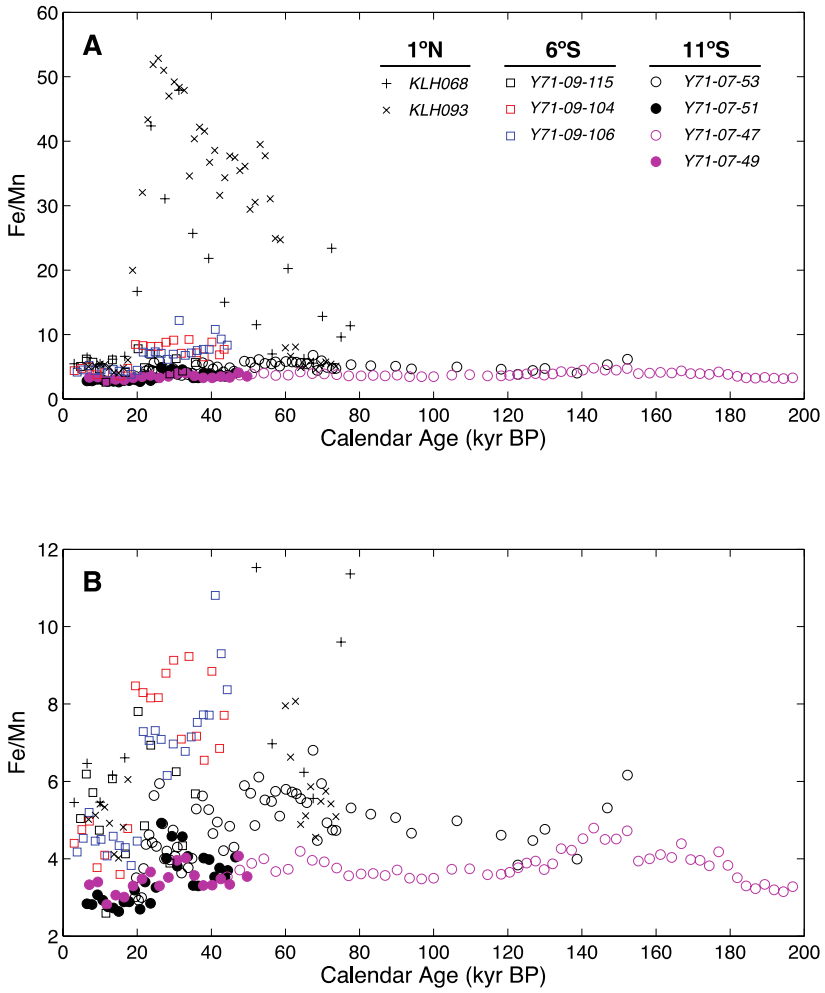

Fig. S7

Fe/Mn ratios vs. time for the EPR cores discussed in the paper. A) Cores at 1ºN (*12*) display Fe/Mn ratios of ~5 from 0-20 kyr BP, with ratios >10 prior to 20 kyr BP. The 6ºS cores display Fe/Mn ratios of 4-5 from 0-20 kyr BP, increasing to 7-9 prior to 20 kyr BP. At 11ºS, Fe/Mn values range from 3-4 throughout each time series, with the exception of Y71-07-53P where Fe/Mn ratios average 5. B) Same as top panel but with expanded y-axis.

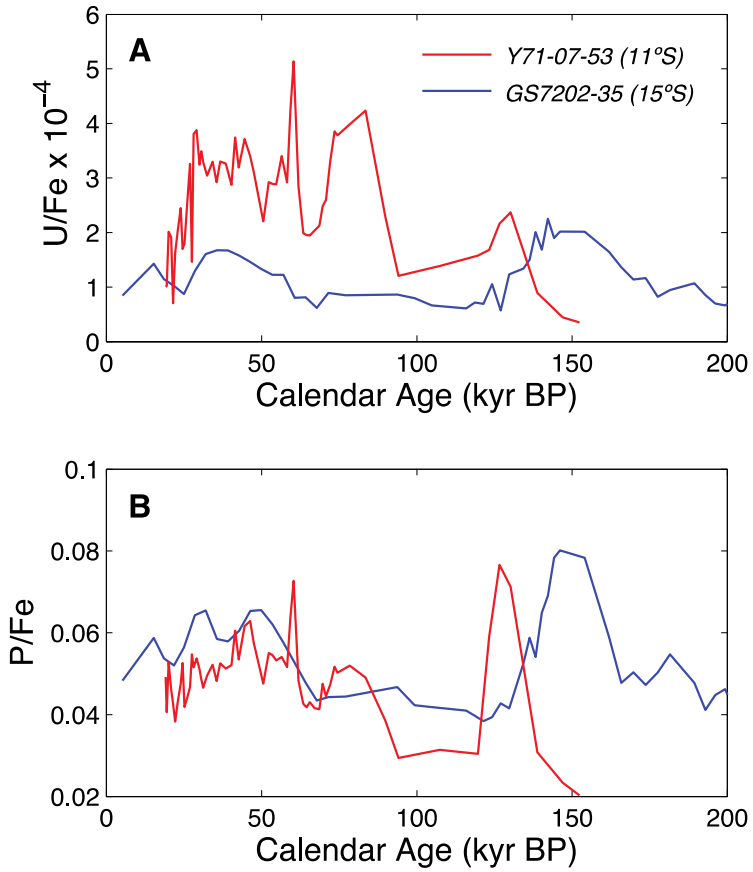

Fig. S8

Published U/Fe and P/Fe ratios for EPR cores at 11ºS and 15ºS. A) U/Fe results for Y71-07-53 at 11ºS (red) (*16*) and GS7202-35 at 15ºS (blue) (*42*). B) P/Fe ratios for the same cores. The age model for Y71-07-53 was developed for this work (see Methhods). In core Y71-07-53, P/Fe peaks during MIS 5 while in core GS7202-35, P/Fe peaks during MIS 6.

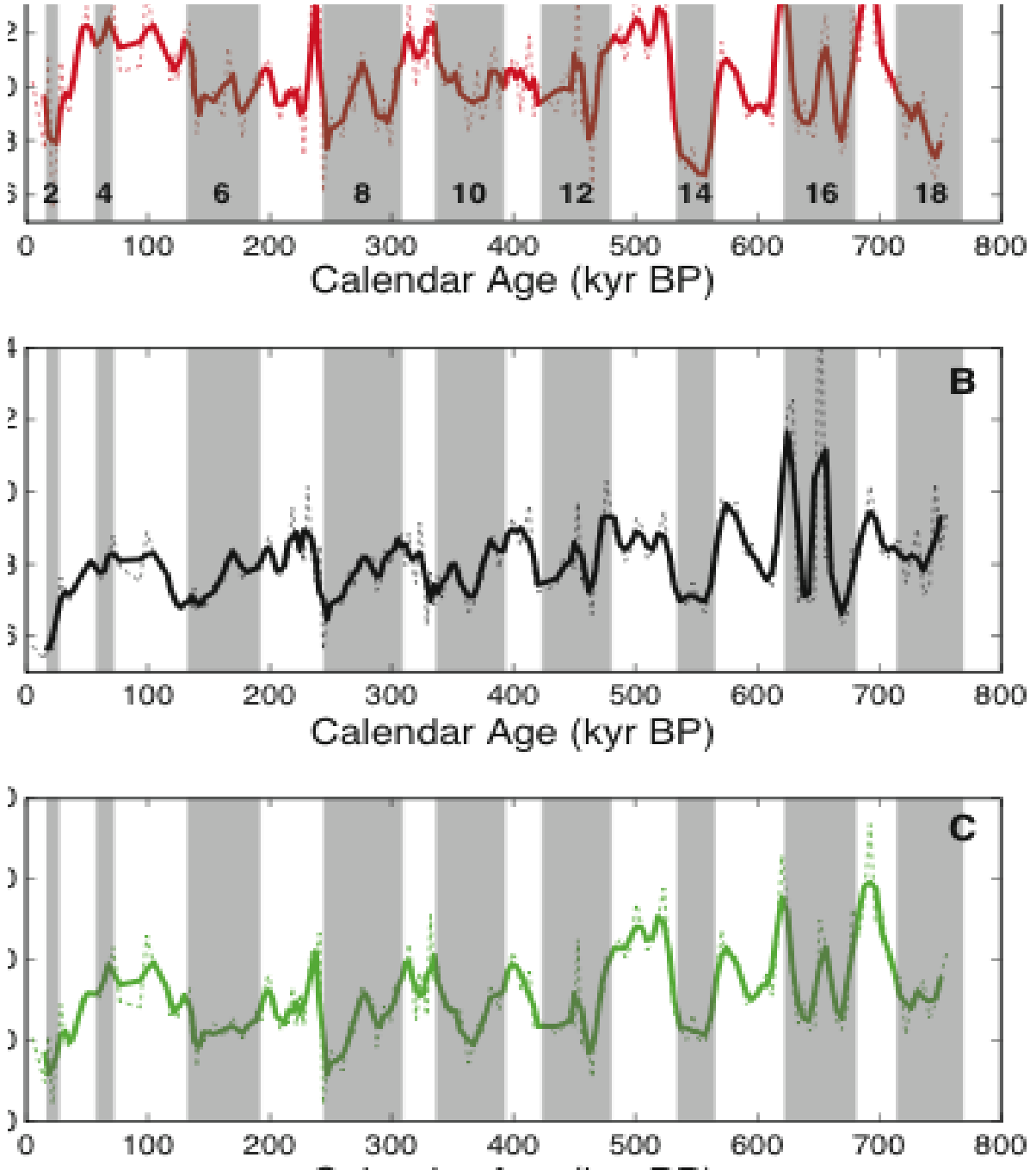

Fig. S9

Metal concentrations for core GS7202-35, expressed on a carbonate free basis (*42*). A) %Fe (cfb), B) %Mn (cfb), and C) ppm V (cfb). The age model is based on correlation of the GS7202-35 bulk $\delta^{18}O$ stratigraphy to a global benthic $\delta^{18}O$ stack (*30*). The approximate time intervals of even numbered Marine Isotope Stages are noted with grey vertical bars.

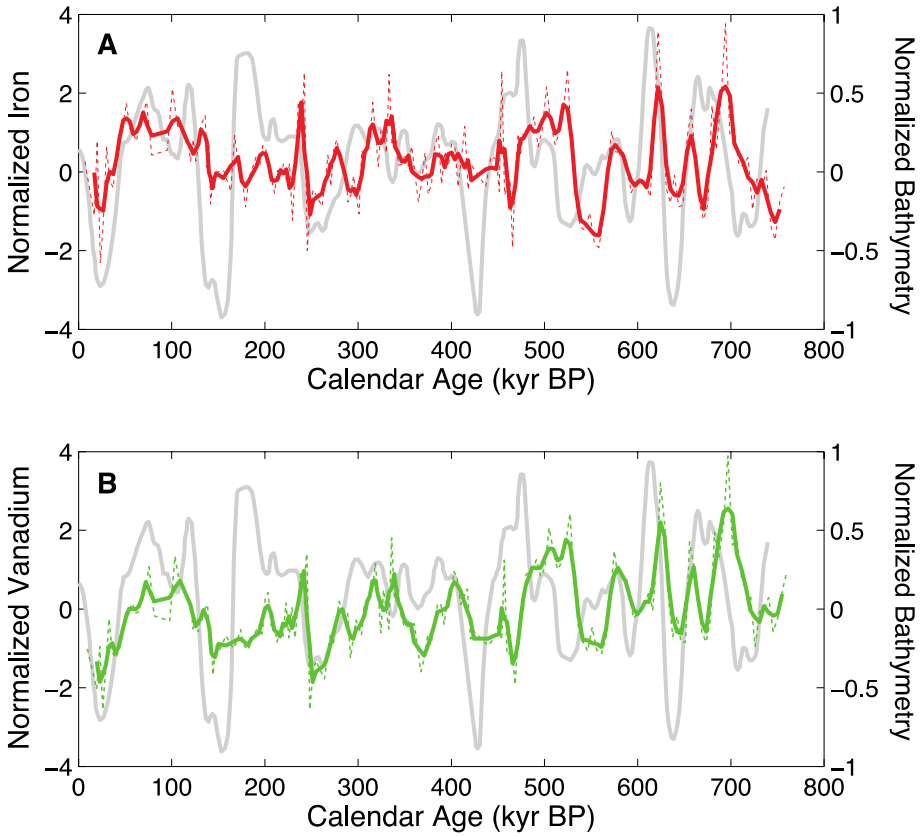

Fig. S10

Hydrothermal sedimentation records from core GS7202-35 (*42*) compared to bathymetry at 17ºS on the EPR (*4*). A) Normalized iron vs. bathymetry, B) Normalized vanadium vs. bathymetry. The carbonate free metal concentration data were normalized by substracting the mean and dividing by the standard deviation of each time series.

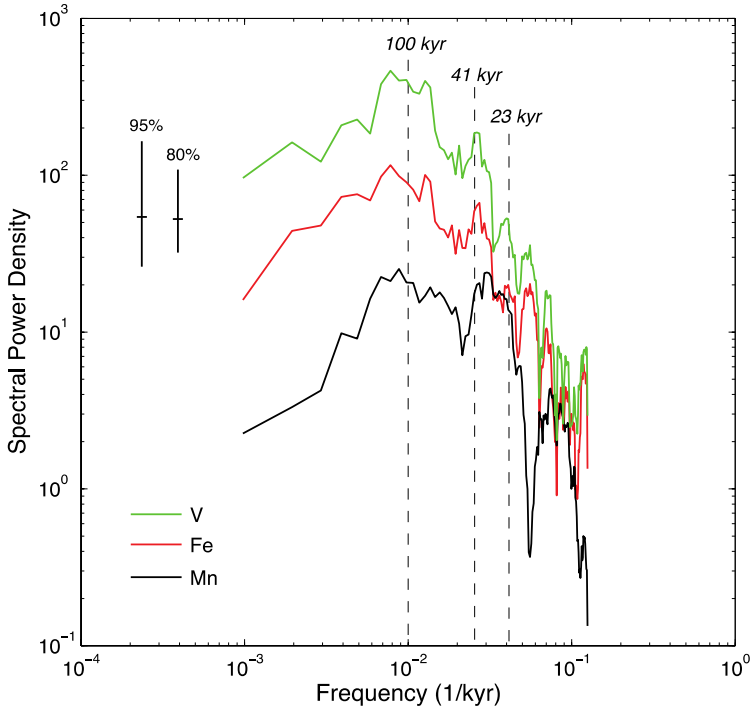

Fig. S11

Multi-taper method (MTM) power spectra for carbonate-free records from GS7202-35, including Fe (red), Mn (black), and V (green). The power spectra were determined using the Matlab MTM routine with 5 windows with a time bandwidth product of 3. The data shown are based on the Thomson adaptive weighting scheme but a simple average produces similar results. 95% and 80% confidence limits are given as vertical bars. Milankovitch periodicities are shown as dashed vertical lines.

Additional Data Table S1 (separate file)
Radiocarbon data

Additional Data Table S2 (separate file)
Oxygen isotope results and age model tie points

Additional Data Table S3 (separate file)
Metal concentrations and %$CaCO_3$ results

Additional Data Table S4 (separate file)
Helium isotopic data

Additional Data Table S5 (separate file)
Correlation matrices for metal flux time series

REFERENCES AND NOTES

1. D. C. Lund, P. D. Asimow, Does sea level influence mid-ocean ridge magmatism on Milankovitch timescales? *Geochem. Geophys. Geosyst.* **12**, Q12009 (2011). doi:10.1029/2011GC003693

2. P. Huybers, C. Langmuir, Feedback between deglaciation, volcanism, and atmospheric CO_2. *Earth Planet. Sci. Lett.* **286**, 479–491 (2009). doi:10.1016/j.epsl.2009.07.014

3. J. W. Crowley, R. F. Katz, P. Huybers, C. H. Langmuir, S. H. Park, Glacial cycles drive variations in the production of oceanic crust. *Science* **347**, 1237–1240 (2015). Medline

4. M. Tolstoy, Mid-ocean ridge eruptions as a climate valve. *Geophys. Res. Lett.* **42**, 1346–1351 (2015). doi:10.1002/2014GL063015

5. E. T. Baker, G. R. German, "On the global distribution of hydrothermal vent fluids," in *Mid-Ocean Ridges: Hydrothermal Interactions Between the Lithosphere and Oceans*, C. R. German, J. Lin, L. M. Parson, Eds. (Geophysical Monograph Series vol. 148, American Geophysical Union, 2004), pp. 245–266.

6. S. E. Beaulieu, E. T. Baker, C. R. German, A. Maffei, An authoritative global database for active submarine hydrothermal vent fields. *Geochem. Geophys. Geosyst.* **14**, 4892–4905 (2013). doi:10.1002/2013GC004998

7. E. T. Baker, Relationships between hydrothermal activity and axial magma chamber distribution, depth, and melt content. *Geochem. Geophys. Geosyst.* **10**, Q06009 (2009). doi:10.1029/2009GC002424

8. J. Dymond, Geochemistry of Nazca plate surface sediments: An evaluation of hydrothermal, biogenic, detrital, and hydrogenous sources. *Geol. Soc. Am.* **154**, 133–174 (1981). doi:10.1130/MEM154-p133

9. G. B. Shimmield, N. B. Price, The scavenging of U, ^{230}Th and ^{231}Pa during pulsed hydrothermal activity at 20°S, East Pacific Rise. *Geochim. Cosmochim. Acta* **52**, 669–677 (1988). doi:10.1016/0016-7037(88)90329-8

10. K. G. Speer, M. E. Maltrud, A. M. Thurnherr, "A global view of dispersion above the mid-ocean ridge," in *Energy and Mass Transfer in Hydrothermal Systems*, P. E. Halbach, V. Tunnicliffe, J. R. Hein, Eds. (Dahlem University Press, 2003), pp. 287–302.

11. K. Boström, M. N. Peterson, O. Joensuu, D. E. Fisher, Aluminum-poor ferromanganoan sediments on active oceanic ridges. *J. Geophys. Res.* **74**, 3261–3270 (1969). doi:10.1029/JB074i012p03261

12. M. Frank, J.-D. Eckhardt, A. Eisenhauer, P. W. Kubik, B. Dittrich-Hannen, M. Segl, A. Mangini, Beryllium 10, Thorium 230, and Protactinium 231 in Galapagos microplate sediments: Implications of hydrothermal activity and paleoproductivity changes during the last 100,000 years. *Paleoceanography* **9**, 559–578 (1994). doi:10.1029/94PA01132

13. Material and methods are available as supplemental materials on *Science* Online.

14. C. R. German, S. Colley, M. R. Palmer, A. Khripounoff, G. P. Klinkhammer, Hydrothermal plume-particle fluxes at 13 degrees N on the East Pacific Rise. *Deep Sea Res. Part I Oceanogr. Res. Pap.* **49**, 1921–1940 (2002). doi:10.1016/S0967-0637(02)00086-9

15. R. R. Cave, C. R. German, J. Thomson, R. W. Nesbitt, Fluxes to sediments underlying the rainbow hydrothermal plume at 36°14′N on the Mid-Atlantic Ridge. *Geochim. Cosmochim. Acta* **66**, 1905–1923 (2002). doi:10.1016/S0016-7037(02)00823-2

16. T. Schaller, J. Morford, S. R. Emerson, R. A. Feely, Oxyanions in metalliferous sediments: Tracers for paleoseawater metal concentrations? *Geochim. Cosmochim. Acta* **64**, 2243–2254 (2000). doi:10.1016/S0016-7037(99)00443-3

17. S. Emerson, J. I. Hedges, "Sediment diagenesis and benthic flux," in *Treatise on Geochemistry*, K. K. Turekian, H. D. Holland, Eds. (Elsevier, vol. 6, 2004), pp. 293–319.

18. J. A. Goff, Comment on "Glacial cycles drive variations in the production of oceanic crust". *Science* **349**, 1065 (2015). Medline doi:10.1126/science.aab2350

19. J. A. Olive, M. D. Behn, G. Ito, W. R. Buck, J. Escartín, S. Howell, Sensitivity of seafloor bathymetry to climate-driven fluctuations in mid-ocean ridge magma supply. *Science* **350**, 310–313 (2015). Medline doi:10.1126/science.aad0715

20. P. U. Clark, A. S. Dyke, J. D. Shakun, A. E. Carlson, J. Clark, B. Wohlfarth, J. X. Mitrovica, S. W. Hostetler, A. M. McCabe, The Last Glacial Maximum. *Science* **325**, 710–714 (2009). Medline doi:10.1126/science.1172873

21. K. Key, S. Constable, L. Liu, A. Pommier, Electrical image of passive mantle upwelling beneath the northern East Pacific Rise. *Nature* **495**, 499–502 (2013). Medline doi:10.1038/nature11932

22. P. B. Kelemen, G. Hirth, N. Shimizu, M. Spiegelman, H. J. B. Dick, A review of melt migration processes in the adiabatically upwelling mantle beneath oceanic spreading ridges. *Philos. Trans. R. Soc. Lond. A* **355**, 283–318 (1997). doi:10.1098/rsta.1997.0010

23. J. Maclennan, M. Jull, D. McKenzie, L. Slater, K. Gronvold, The link between volcanism and deglaciation in Iceland. *Geochem. Geophys. Geosyst.* **3**, 1–25 (2002). doi:10.1029/2001GC000282

24. P. Cartigny, F. Pineau, C. Aubaud, M. Javoy, Towards a consistent mantle carbon flux estimate: Insights from volatile systematics (H_2O/Ce, δD, CO_2/Nb). *Earth Planet. Sci. Lett.* **265**, 672–685 (2008). doi:10.1016/j.epsl.2007.11.011

25. J. M. A. Burley, R. F. Katz, Variations in mid-ocean ridge CO_2 emissions driven by glacial cycles. *Earth Planet. Sci. Lett.* **426**, 246–258 (2015). doi:10.1016/j.epsl.2015.06.031

26. M. Hofmann, M. A. Morales Maqueda, Geothermal heat flux and its influence on the oceanic abyssal circulation and radiocarbon distribution. *Geophys. Res. Lett.* **36**, L03603 (2009). doi:10.1029/2008GL036078

27. J. Emile-Geay, G. Madec, Geothermal heating, diapycnal mixing and the abyssal circulation. *Ocean Sci.* **5**, 203–217 (2009). doi:10.5194/os-5-203-2009

28. P. Martin, D. Archer, D. W. Lea, Role of deep sea temperature in the carbon cycle during the last glacial. *Paleoceanography* **20**, PA2015 (2005). doi:10.1029/2003PA000914

29. D. K. Smith, H. Schouten, L. Montési, W. Zhu, The recent history of the Galapagos triple junction preserved on the Pacific plate. *Earth Planet. Sci. Lett.* **371–372**, 6–15 (2013). doi:10.1016/j.epsl.2013.04.018

30. L. E. Lisiecki, M. E. Raymo, A Pliocene-Pleistocene stack of 57 globally distributed benthic delta O-18 records. *Paleoceanography* **20**, PA1003 (2005).

31. W. S. Broecker, E. Clark, An evaluation of Lohmann's foraminifera weight dissolution index. *Paleoceanography* **16**, 531–534 (2001). doi:10.1029/2000PA000600

32. R. N. Sortor, D. C. Lund, No evidence for a deglacial intermediate water $\Delta^{14}C$ anomaly in the SW Atlantic. *Earth Planet. Sci. Lett.* **310**, 65–72 (2011). doi:10.1016/j.epsl.2011.07.017

33. A. Koutavas, J. Lynch-Stieglitz, Glacial-interglacial dynamics of the eastern equatorial Pacific cold tongue-intertropical convergence zone system reconstructed from oxygen isotope records. *Paleoceanography* **18**, 1089 (2003). doi:10.1029/2003PA000894

34. T. O. Rooney, W. K. Hart, C. M. Hall, D. Ayalew, M. S. Ghiorso, P. Hidalgo, G. Yirgu, Peralkaline magma evolution and the tephra record in the Ethiopian rift. *Contrib. Mineral. Petrol.* **164**, 407–426 (2012). doi:10.1007/s00410-012-0744-6

35. R. M. Dunk, R. A. Mills, The impact of oxic alteration on plume-derived transition metals in ridge flank sediments from the East Pacific Rise. *Mar. Geol.* **229**, 133–157 (2006). doi:10.1016/j.margeo.2006.03.007

36. B. Schramm, C. W. Devey, K. M. Gillis, K. Lackschewitz, Quantitative assessment of chemical and mineralogical changes due to progressive low-temperature alteration of East Pacific Rise basalts from 0 to 9 Ma. *Chem. Geol.* **218**, 281–313 (2005). doi:10.1016/j.chemgeo.2005.01.011

37. H. Snoeckx, D. K. Rea, Late quaternary $CaCO_3$ stratigraphy of the eastern equatorial Pacific. *Paleoceanography* **9**, 341–351 (1994). doi:10.1029/93PA03023

38. F. Marcantonio, S. Higgins, R. F. Anderson, M. Stute, P. Schlosser, E. T. Rasbury, Terrigenous helium in deep-sea sediments. *Geochim. Cosmochim. Acta* **62**, 1535–1543 (1998). doi:10.1016/S0016-7037(98)00091-X

39. K. A. Farley, A. Montanari, R. Coccioni, A record of the extraterrestrial ^3He flux through the late cretaceous. *Geochim. Cosmochim. Acta* **84**, 314–328 (2012). 10.1016/j.gca.2012.01.015 doi:10.1016/j.gca.2012.01.015

40. D. B. Patterson, K. A. Farley, Extraterrestrial ^{3}He in seafloor sediments: Evidence for correlated 100 kyr periodicity in the accretion rate of interplanetary dust, orbital parameters, and quaternary climate. *Geochim. Cosmochim. Acta* **62**, 3669–3682 (1998). doi:10.1016/S0016-7037(98)00263-4

41. V. Marchig, J. Erzinger, P. Heinze, Sediment in the black smoker area of the East Pacific Rise (18.5°S). *Earth Planet. Sci. Lett.* **79**, 93–106 (1986). doi:10.1016/0012-821X(86)90043-9

42. R. A. Mills, S. L. Taylor, H. Palike, J. Thomson, Hydrothermal sediments record changes in deep water oxygen content in the SE Pacific. *Paleoceanography* **25**, PA4226 (2010). doi:10.1029/2010PA001959

43. J. L. Morford, S. Emerson, The geochemistry of redox sensitive trace metals in sediments. *Geochim. Cosmochim. Acta* **63**, 1735–1750 (1999). doi:10.1016/S0016-7037(99)00126-X

44. B. P. Finney, M. W. Lyle, G. R. Heath, Sedimentation at Manop Site H (Eastern Equatorial Pacific) over the past 400,000 years: Climatically induced redox variations and their effects on transition metal cycling. *Paleoceanography* **3**, 169–189 (1988). doi:10.1029/PA003i002p00169

45. M. Lyle, A brown-green transition in marine sediments: A marker of the Fe (III)-Fe(II) redox boundary. *Limnol. Oceanogr.* **28**, 1026–1033 (1983). doi:10.4319/lo.1983.28.5.1026